Fabrication of a side aligned optical fibre interferometer by focused ion beam machining

Fabrication of a side aligned optical fibre interferometer by focused ion beam machining

2013 J. Micromech. Microeng. 23 105005

(http://iopscience.iop.org/0960-1317/23/10/105005)

OPEN ACCESS
IOP PUBLISHING
Made open access 24 March 2014
JOURNAL OF MICROMECHANICS AND MICROENGINEERING
J. Micromech. Microeng. **23** (2013) 105005 (9pp)
doi:10.1088/0960-1317/23/10/105005

Fabrication of a side aligned optical fibre interferometer by focused ion beam machining

J Sun[1,4], J Li[2], R R J Maier[2], D P Hand[2], W N MacPherson[2], M K Miller[1], J M Ritchie[1] and X Luo[1,3]

[1] Institute of Mechanical, Process and Energy Engineering, Heriot-Watt University, Edinburgh, EH14 4AS, UK
[2] Institute of Photonics and Quantum Sciences, Scottish Universities Physics Alliance, Heriot-Watt University, Edinburgh, EH14 4AS, UK
[3] Department of Design, Manufacture and Engineering Management, University of Strathclyde, Glasgow, G4 0NG, UK

E-mail: Jining.Sun@hw.ac.uk

Received 27 May 2013, in final form 14 August 2013
Published 5 September 2013
Online at stacks.iop.org/JMM/23/105005

Abstract
Focused ion beam (FIB) machining is a promising technique for the fabrication of micro-optical components with high quality surface finishes. In this work, a prototype of a side aligned optical fibre interferometer was successfully fabricated by the three-dimensional deterministic FIB machining technique. A highly accurate 45° reflective mirror with surface roughness (Ra) of 10 nm has been successfully fabricated at the centre of the fibre to direct the core guided light to the side of the fibre. A surface topography simulation method was developed to simulate the ion beam polishing process. According to the simulation result, a 0.5° offset on the ion beam polishing direction is necessary to maintain the machining accuracy. In the fabrication process, it was also found that for structures requiring a high aspect ratio the existence of an open edge can mitigate against the material redeposition on the sidewalls and therefore increase the overall material removal rate. The fibre has been tested optically and the interference signals have been successfully observed, demonstrating the alignment accuracy of the fabrication method.

(Some figures may appear in colour only in the online journal)

1. Introduction

Since the development of practical optical fibres in the 1960s, they have been explored as possible sensors because of their ability to guide light in a well-controlled manner. Optical fibre based sensors have benefits over electrical sensors which are relevant for applications in sensor miniaturization, insensitivity to electrical interference and multiplexing ability. Recently, significant effort has been put into utilising optical fibres for practical applications [1]; sensing solutions are also becoming commercially available, in particular concepts based fibre Bragg gratings [2] and distributed measurement systems [3].

There are several approaches to using optical means for measurement, such as intensity based sensors, grating based sensors, and interferometers. Interferometry offers potential for high measurement sensitivity with resolution on the scale of the wavelength of light. For example, successful fibre interferometers have been demonstrated for measuring subsea acoustic signatures via fibre hydrophone arrays [4]. Interferometry is increasingly being used for interrogating fibre tip sensors. Of the many interferometer configurations available, three interferometer designs including the Michelson, Mach–Zehnder and Fabry–Perot interferometers are commonly used in sensing applications [5–7]. In this paper we exploit the Fabry–Perot configuration because of the advantage that the interferometer is connected to the

[4] Author to whom any correspondence should be addressed.

interrogation system by a single fibre. This is suitable for probe-type sensors and, more importantly, the connecting lead is rendered insensitive to perturbation from external factors.

A typical Fabry–Perot cavity is formed between two parallel reflective mirrors. This can be used as a sensor because the reflection (or transmission) spectrum features are a function of the spacing between the cavity mirrors. This approach has been used for many sensors using thin optical films [7] and external sensor cavities [8]. One challenge with producing these cavities is to fabricate reliable, well-aligned, and miniaturized structures. The ideal configuration would be a monolithic structure to minimize alignment errors associated with attaching sensing components. Fabrication can be simplified by reducing the component count and thereby reducing, or eliminating, any alignment requirements between parts, i.e. by fabricating the Fabry–Perot cavity from a single optical fibre [9]. In principle, the key to meet all of the above requirements is to create a cavity microstructure with a pair of parallel sidewalls. This approach has been exploited elsewhere to produce miniaturized interferometers, such as micro cantilever sensors [9–12]. In such applications, the parallel reflective mirrors are perpendicular to the fibre core and therefore only the changes along the fibre axis are detected. Here our interest is to fabricate sensors in which the sensing direction is perpendicular to the fibre axis, i.e. to build a sensor interferometer onto the side of an optical fibre.

Micromachining techniques have been reported as capable of fabricating optical cavities in optical fibres, for example focused ion beam (FIB) machining [3] has been shown to be capable of machining sensing structures on fibre end tips. FIB machining is highly suitable for micro-fabrication due to its small spot size and stable operating conditions [13]. It utilizes a beam of high energy ions to bombard substrate atoms where the collision transfers sufficient energy to the substrate atoms to overcome the surface binding energy leading to a physical sputtering effect. This technique has been extensively used in a number of fibre-based applications, including the modification of waveguide properties [14], fabrication of long period gratings [15], micromachining of a micro-notch cavity on the fibre tip for interferometric sensing [10], etching nanostructures on the end-faces of optical fibres for chemical sensing [16], and the precision cutting of photonic crystal fibres [17]. In 2006, Iannuzzi *et al* firstly demonstrated that FIB machining can be used for the fabrication of two-dimensional (2D) structures on tips of optical fibres to form a monolithic fibre-top sensor [9], which proofs the possibility of FIB machined monolithic structures in optical fibre sensing applications. Such monolithic configuration greatly eliminates the alignment requirements and can be widely used as optomechanical transducers [18], temperature sensors [9], hydrogen sensors [19], and atomic force microscopes [10, 20]. However, the fabrication of three-dimensional (3D) structures with high accuracy on optical fibres remains challenging. 3D structure on an optical fibre can provide potential sensing applications in acceleration measurement and *in-vivo* medical devices etc. with extra or enhanced sensing capabilities.

It is difficult to obtain accurate 3D structures from the ion beam machining process due to stochastic errors arising from the ion beam overlap effect, beam tail effect, angular dependence of the sputter yield, and re-deposition effect [21, 22]:

- Due to the scattering of the ions emitted from the liquid metal ion source and the limitation in the focusing capability of the ion column, the ion beam has a finite size and is usually considered as a Gaussian distribution with a circular cross section. In order to form a smooth surface, the pixel spacing of the scanning ion beam has to be smaller than the ion beam size. Consequently this produces an *overlap effect*—an extra ion dose from the adjacent pixels to contribute to the local milling pixel. Therefore, the actual ion dose received at a local pixel is higher than the desired ion dose; for this reason the machined surface diverges from the designed shape.
- The *beam tail effect* is another side effect that originated from the nature of Gaussian beams. The tail of the Gaussian beam brings an extra ion dose around the machining point. Depending on the scanning strategy, the extra ion dose forms round corners, blunt edges, and inclined side walls, which degrade the machining form accuracy.
- The *sputter yield* indicates the total number of sputtered atoms per incident ion particle and this is shown to be a function of the angle between the incident ions and the target surface. During fabrication of 3D structures, the ions bombard the target surface in a constant incident angle while the local surface slope may change as a result of material sputtering; therefore, the sputter yield changes as a function of the machining time.
- The *redeposition effect* accompanies the ion sputtering process. Some of the sputtered atoms formed by the incident ion beam will redeposit at the site of interest thereby reducing the net removal rate and creating unwanted features.

Several methods have been reported regarding fabrication of 3D structures by FIB machining. Vasile *et al* introduced a depth control method by controlling the dwell time on each milling pixel [23, 24]. In this method, a general mathematical model was developed which directs the ion beam material removal process and has the capability of milling a 3D cavity from a given initial geometry into a pre-specified final geometry. Fu *et al* [25] employed a 2D slice-by-slice method to fabricate 3D structures by FIB. Sequential 2D slices with small thicknesses were used to approach the desired 3D structures. Similarly, Lalev *et al* [26] developed a data preparation program for FIB machining of complex 3D structures utilizing this slice-by-slice method. Sun *et al* [27] applied a divergence compensation method to carve 3D structures by using a series of bitmaps. This method was implemented in FIB machining by transferring the dwell time information onto a series of bitmaps which can be easily recognized by the system. To the authors' knowledge none of these techniques has ever been applied to machining structures on optical fibres.

In this work, we present a fibre-side interferometer sensor directly fabricated by FIB machining. A sketch of the fibre-side interferometer sensor is shown in figure 1. A high

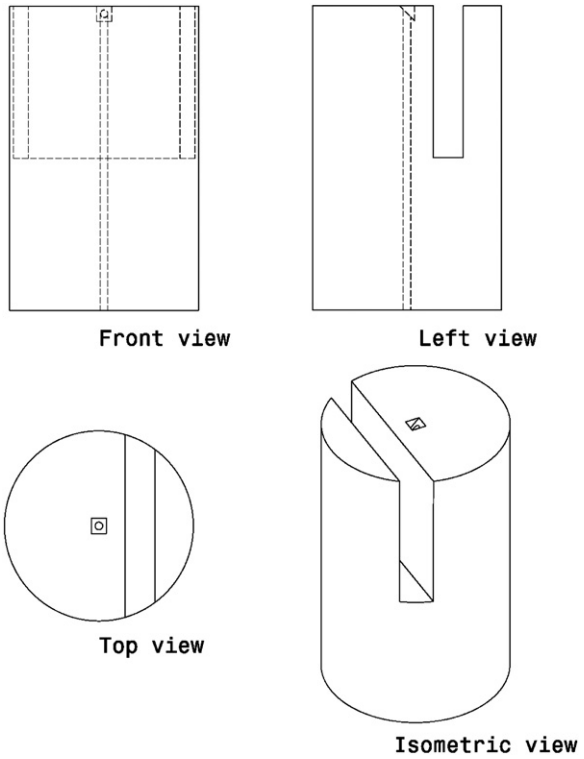

Figure 1. Three-view drawings of the fibre-side interferometer sensor.

aspect-ratio (∼20:1) channel with parallel sidewalls is machined on the side of the fibre to form the Fabry–Perot cavity. A micro 45° reflective mirror aligned to the core of the fibre is then carved using the divergence compensation method, followed by an ion polishing process to allow light from the core to optically access the sensor cavity. Such 45° angled mirrors have been produced on the ends of fibres previously, for example by polishing [28], however this is only applicable when fabricating the reflective mirror on single core fibres. The FIB machined micro 45° reflective mirror may have future application with multi-core fibres to enable the mirror alignment to be different for each of the cores allowing flexibility in setting the beam directions. However, here we restrict our investigation to a single core sensor.

2. Fabrication of the fibre-side sensor

A standard fused silica single-mode optical fibre with an outer (cladding) diameter of 125 μm and a light guiding core diameter of ∼9 μm was coated with a 20 nm thick layer of aluminium to reduce electrostatic charge accumulation on the machined parts of the fibre. The fibre was then mounted on a custom metallic block containing an alignment 'V' groove to accurately locate and hold the fibre. The FIB machining was carried out using a dual-beam FIB system (FEI Quanta 3D FEG) which contains a liquid gallium ion source and a field emission scanning electron microscope (SEM). The fibre mounting block, together with the optical fibre, was fixed on to a 5-axis motorized stage with 300 nm positional resolution and 360° rotational range. The stage can tilt in the electron–ion beam plane from −15° to +75° with 0.1° resolution.

2.1. Fabrication of the optical cavity

The prepared fibre is positioned such that the ion beam can machine the side of the fibre. The SEM (aligned at 38.0° angle relative to the fibre side) is available for real-time monitoring of the fabrication process. This experimental setup is illustrated in figure 2(*a*). The acceleration voltage of the FIB was held constant at 30 keV throughout the machining process. In order to remove a large block of materials (450 × 20 × 100 μm^3) on the side of the fibre, a high current intensity of 50 nA with a beam spot size of 300 nm was used. This removed volume serves as the optical cavity for the sensor, and therefore the sidewalls in the cavity need to be strictly parallel with each other to ensure sufficient reflected signals can be coupled back into the fibre core for detection. Unfortunately, it is known that an amorphous layer can be formed on FIB machined sidewalls due to the redeposition effect [29]. In order to minimize the redeposition and increase the machining efficiency, the ion beam scanning commenced 2 μm away from the edge of the top surface as it is shown in figure 2(*a*), forming one open edge, from which machining debris can easily escape. Details on the scanning strategy are discussed in later sections. Subsequent to the main material removal process we 'polish' the sidewalls with 7 nA ion current to achieve parallel walls and a smooth surface finish. In order to mitigate material redeposition, the pair of sidewalls was alternately polished with ion beams of increasingly smaller cross sections, ending with 44 nm diameter and 1 nA ion current.

2.2. Fabrication of the 45° reflective mirror

To optimize the FIB milling process, a predictive divergence compensation approach is applied to fabricate the 45° reflective mirror. The machining area was discretized by the number of milling pixels. The milling depth at each pixel is derived from the ion incident flux, atom density of the target material, and sputter yield. The total incident flux at a certain pixel is contributed not just from the local pixel area but also from all of the adjacent areas due to the overlap effect. Therefore, the dwell time, t_{kl}, for each node can be obtained from a matrix relationship as shown in equation (1), which includes the ion beam distribution, ion beam overlap, and angular-dependent sputter yield [27]:

$$\Delta Z_{i,j} = \sum_{k,l=1}^{N} \frac{\Phi(k,l)}{\eta} J_{kl}(i,j) Y(\theta_{ij}) \cos(\theta_{ij}) t_{kl} p_x p_y, \qquad (1)$$

where $\Phi(k, l)$ is the ion flux density at node (k, l). η and J_{kl} are the atom density of fused silica and the ion beam intensity distribution function at node (k, l), respectively. Generally J_{kl} follows Gaussian distribution. $Y(\theta)$ is the angular-dependent sputter yield which is determined by a Monte Carlo simulation. θ_{ij} is the separation angle between the incident ion beam and the surface normal at node (i, j). $\Delta Z_{i,j}$ is the depth at node (i, j) where p_x and p_y represent the pixel spacing along the x and y directions, respectively. The summation over the indices k and l accounts for total dose received at node (i, j) from all the pixels in the address scheme. Equation (1) can be applied to each pixel in the machining area to obtain a corrected FIB milling depth. In an area comprising of $N \times N$ pixels, the

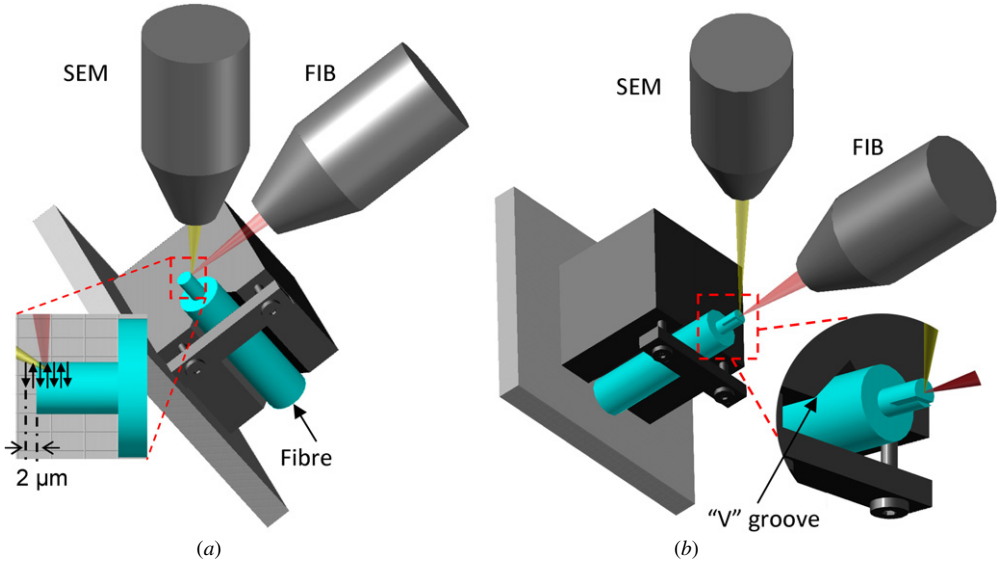

Figure 2. Experimental setup of the FIB machining process: (*a*) the fabrication of the Fabry–Perot cavity by side machining of the fibre; the incident ion beam is perpendicular to the fibre length direction; (*b*) fabrication of the 45° reflective mirror on the fibre end face; the ion beam is incident along the fibre axis.

total milling time $p_{kl}t_{kl}$ at each pixel is derived from $N \times N$ equation sets composed of equation (1). Therefore, the dwell time distribution is calculated by:

$$t = Z/C, \tag{2}$$

where t and Z are dwell time matrix and milling depth matrix, respectively. C is the coefficient matrix of the equation set.

In this stage the ion source was operated at an acceleration voltage of 30 kV. The beam diameter and the ion current are 66 nm and 3 nA. In the ion beam scanning process, the pixel spacing was set to half of the beam diameter (33 nm). This can be controlled by assigning a bitmap with 302 × 302 pixels to a 10 × 10 μm^2 milling area. The dwell time at each beam position was calculated according to equation (2), with the consideration of the beam overlap effect and the angular dependence of sputter yield. A 10 × 10 μm reflective mirror with 45° inclined angle to the fibre core was successfully obtained after 52 scanning passes with a maximum dwell time of 255 μs. The result of this process is shown in figure 3(*a*). Figure 3(*b*) schematically shows the ion dose exposure process when fabricating the reflective mirror.

2.3. Ion beam polishing process

Off-normal incident ion-bombardment of solid surfaces is known to cause the formation of periodically modulated structures often referred to as ripples [30]. Such ripples on the reflective mirror will affect the optical path and, therefore, it is desirable to eliminate them. The wavelength of these ripples typically depends on the ion incident angle; according to Bradley and Harper's theory [30], the wavelength approaches infinite when the ion incident angle approaches 90° to the surface normal. That is to say that ideally a ripple-free surface can be formed when the ion incident angle is 90°. Therefore, an ion beam polishing process is helpful in eliminating the ripples on the mirror. Here we polish with the ion beam incident along surface of the reflective mirror with a current of 1 nA. In order to compensate for the Gaussian profile of the incident ion beam, the polishing angle was offset by 0.5° with respect to the surface of the reflective mirror as shown in figure 4(*a*). A layer of platinum was then coated onto the mirror surface by FIB induced deposition to increase the mirror reflectivity. The SEM images of the reflective mirror are shown in figures 4(*b*) and (*c*). The overall image of the fibre-side optic sensor is shown in figure 4(*d*).

3. Results and discussions

3.1. Calculation of the material removal rate

The machining efficiency in the FIB nanofabrication process depends on the sputter yield, therefore the sputter yield of fused silica under various incident angles needs to be determined. In this work, this was calculated using a Monte Carlo simulation code-TRIDYN [31, 32]. The calculations modelled impingement of 30 keV gallium ions onto a flat surface. In this simulation, the choice of the surface binding energy of the target atoms is critical to the sputter yield. When a SiO_2 molecule was sputtered out of the surface, the conservation of energy requires:

$$\mathrm{SBE_{Si}} + 2 \times \mathrm{SBE_O} = \Delta H^s_{\mathrm{Si}} + \Delta H^f_{\mathrm{SiO_2}} + \Delta H^{\mathrm{diss}}_{\mathrm{O_2}}, \tag{3}$$

where $\mathrm{SBE_{Si}}$ and $\mathrm{SBE_O}$ represents the surface binding energy of Si and O atoms;ΔH^s_{Si}, $\Delta H^f_{\mathrm{SiO_2}}$, and $\Delta H^{\mathrm{diss}}_{\mathrm{O_2}}$ denotes the enthalpy of sublimation, formation, and dissociation, respectively.

A proper choice of the surface binding energies is

$$\mathrm{SBE_{Si}} = \Delta H^s_{\mathrm{Si}}, \tag{4}$$

$$\mathrm{SBE_O} = \tfrac{1}{2}\Delta H^f_{\mathrm{SiO_2}} + \tfrac{1}{2}\Delta H^{\mathrm{diss}}_{\mathrm{O_2}}. \tag{5}$$

With $\Delta H^s_{\mathrm{Si}} = 4.70$ eV, $\Delta H^f_{\mathrm{SiO_2}} = 9.44$ eV, and $\Delta H^{\mathrm{diss}}_{\mathrm{O_2}} = 5.15$ eV, it is reasonable to set $\mathrm{SBE_{Si}} = 4.7$ eV and $\mathrm{SBE_O} =$

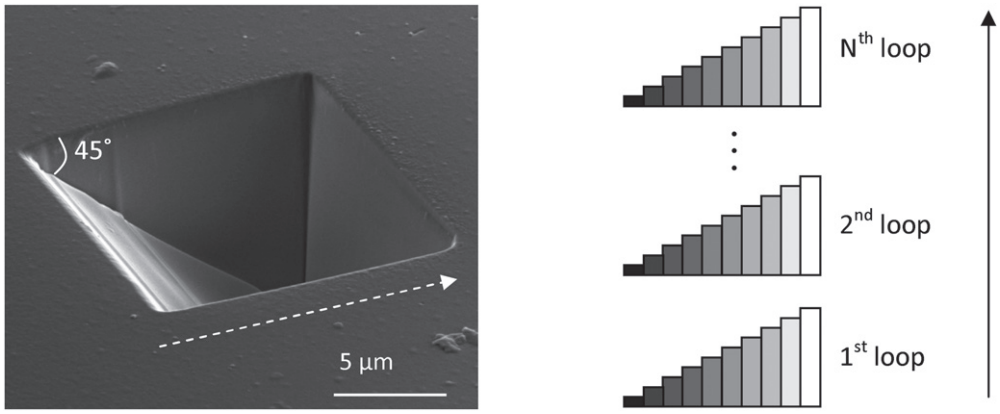

(*a*) (*b*)

Figure 3. The 45° reflective mirror caved on top of the fibre (*a*) and the total exposure dose used for experiments with *N* exposure loops (*b*). Rectangles in (*b*) represent exposure elements corresponding to cross sections along dot–arrow of (*a*). Vertical arrow in (*b*) shows exposure order.

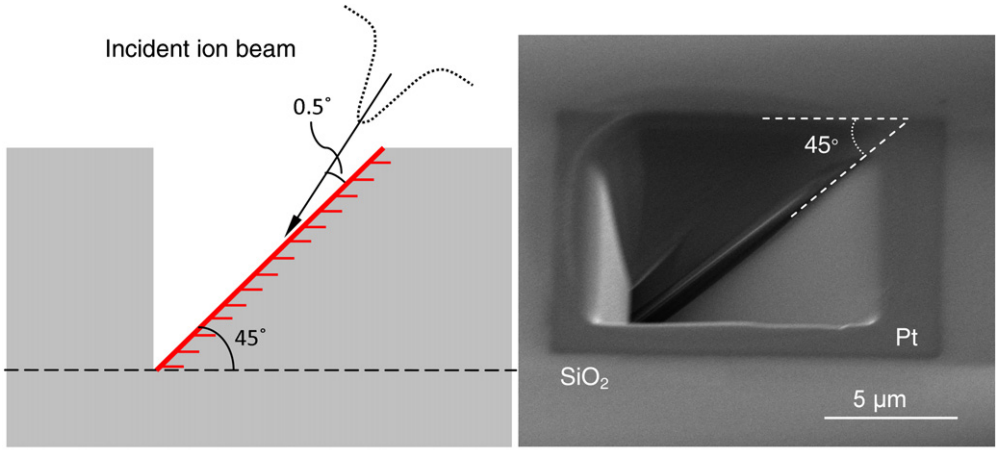

(*a*) (*b*)

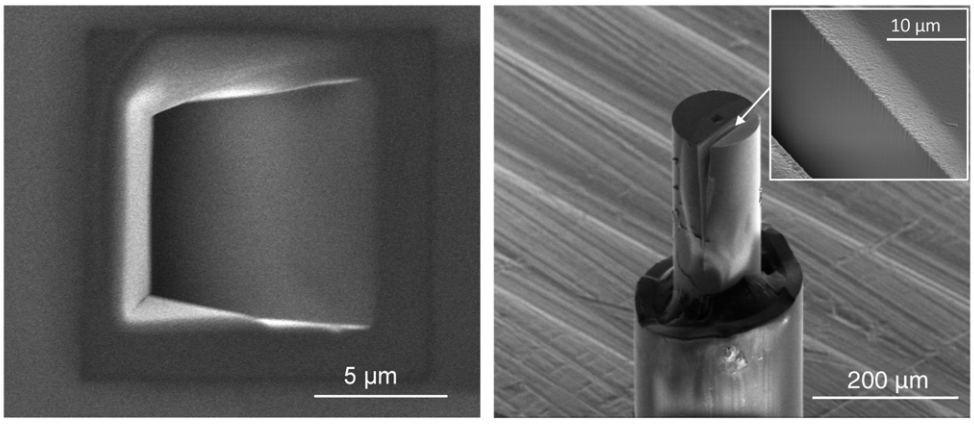

(*c*) (*d*)

Figure 4. The 45° reflective mirror caved at the centre of the optical fibre. (*a*) A sketch of the ion polishing process; (*b*) and (*c*) show SEM images of the 45° reflective mirror viewed from 52° and 0°; (*d*) the overall SEM image of the fibre-side optic sensor.

7.30 eV. Simulation results indicate that the sputter yield is 1.88 atoms/ion (0.65 silicon atoms and 1.23 oxygen atoms) when the ion incident angle is 0° with an ion current of 1 nA. The sputter yield keeps increasing as the ion incident angle until 83°, where the sputter yield reaches the maximum 17.65 atoms/ion (5.70 silicon atoms and 11.97 oxygen atoms).

When fabricating the Fabry–Perot cavity, the ion beam scanning started 2 μm away from the edge of the top surface and then moved towards the fibre as it is shown in figure 1(*a*). The open edge of the cavity was formed by applying this scanning strategy. The existence of the open edge boosts the material removal rate, particularly when fabricating structures with a high aspect-ratio. The sputtered atoms cannot only escape from the top surface of the cavity (the incident ion beam direction), but also from the open edge. Therefore, the redeposition effect was suppressed. Figure 5 compares the

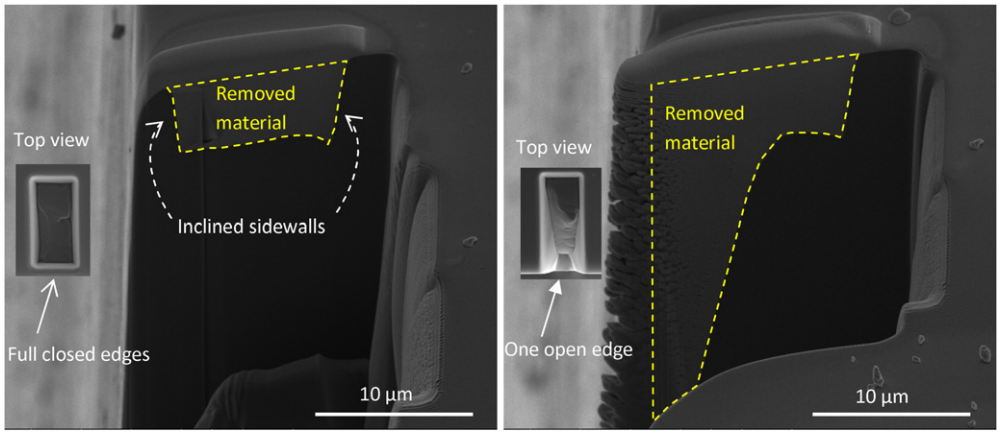

(*a*) (*b*)

Figure 5. Cross-sectional view of the cavities fabricated using an ion current of 5 nA (design cavity top cross section area: 5 μm $\times$ 10 μm with a sputtering time of 300 s): (*a*) with fully enclosed edges and (*b*) with one open edge.

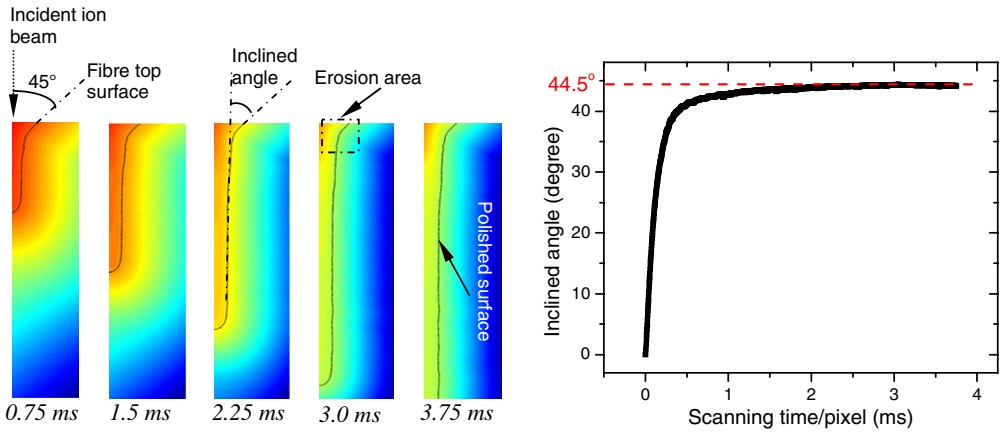

(*a*) (*b*)

Figure 6. The level set functions (*a*) and the inclined angle of the polished edge (*b*) when fabricated by a beam of ions with a current of 1 nA.

differences between the geometrical cavities with full edges and one open edge sputtered by FIB machining with identical machining parameters. Both of the cavities were formed on the edge of a fused silica substrate with an ion current of 5 nA. Figure 5 shows that the removed material in the cavity with one open edge is 2.3 times more than the cavity with full edges. The bottom part near the open edge collapsed during the fabrication. This phenomenon yielded an increase in the incident angle of the ion beam, which further boosted the sputter yield. Therefore, the formation of the open edge in the machining process is of great benefit to boost machining efficiency. In this work, the total machining time of the Fabry–Perot cavity is 3 h, which is one third of the machining time taken to fabricate the cavity with fully closed edges.

3.2. Compensation of the beam tail effect

As discussed earlier, the ion beam intensity profile is non-uniform and approximately follows a Gaussian distribution. As a result of this it is very difficult to fabricate vertical sidewalls in FIB machined structures. This is illustrated in figure 5(*a*) where both sidewalls are inclined towards the centre of the cavity because of this effect. The same phenomenon also appears in the ion beam polishing process, in which case the direction of the polished sidewall is not coincident with the incident ion beam direction.

In our application, it is important that the mirror is correctly aligned (i.e. 45° to the fibre axis, with correct alignment towards the sensor cavity) as misalignment will significantly affect the return signal. Therefore, the angle of the reflective mirror must be precisely controlled hence the contribution from the beam tail effect associated with the ion polishing process should be well understood and compensated for as required. We evaluated the contribution from beam tail effect quantitatively by a surface topography simulation approach based on a level set method. The level set method [33] is a numerical technique for tracking the evolution of interfaces and shapes, in our case as the machining process proceeds. The advantages of this method are that one can perform numerical computations involving curves and surfaces on a fixed Cartesian grid without having to parameterize these objects, and the topological merging and breaking, sharp gradients, and cusps can form naturally. The central mathematical idea of level set method is to view the moving front as a particular level set of a higher dimensional level set function Φ. The actual moving front (x, y, t) is designed

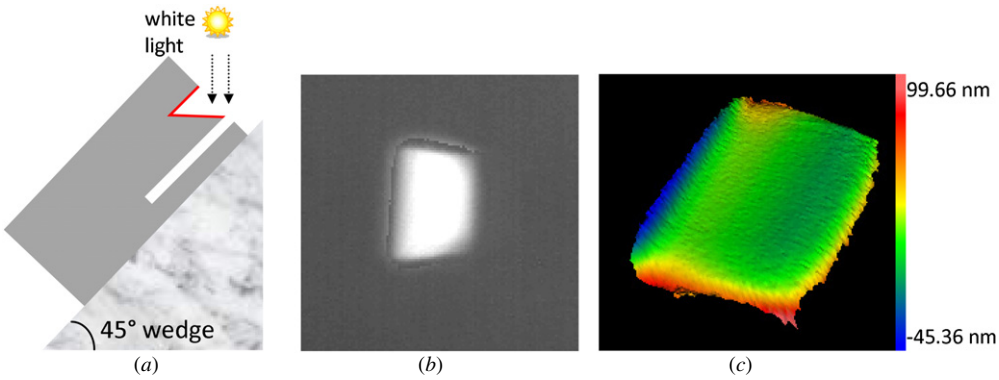

Figure 7. The measurement of a polished 45° reflect mirror by a white light interferometer: (*a*) sketch of the fibre alignment; (*b*) an image of the reflective mirror captured by the optical camera; (*c*) measurement result of the 45° reflective mirror.

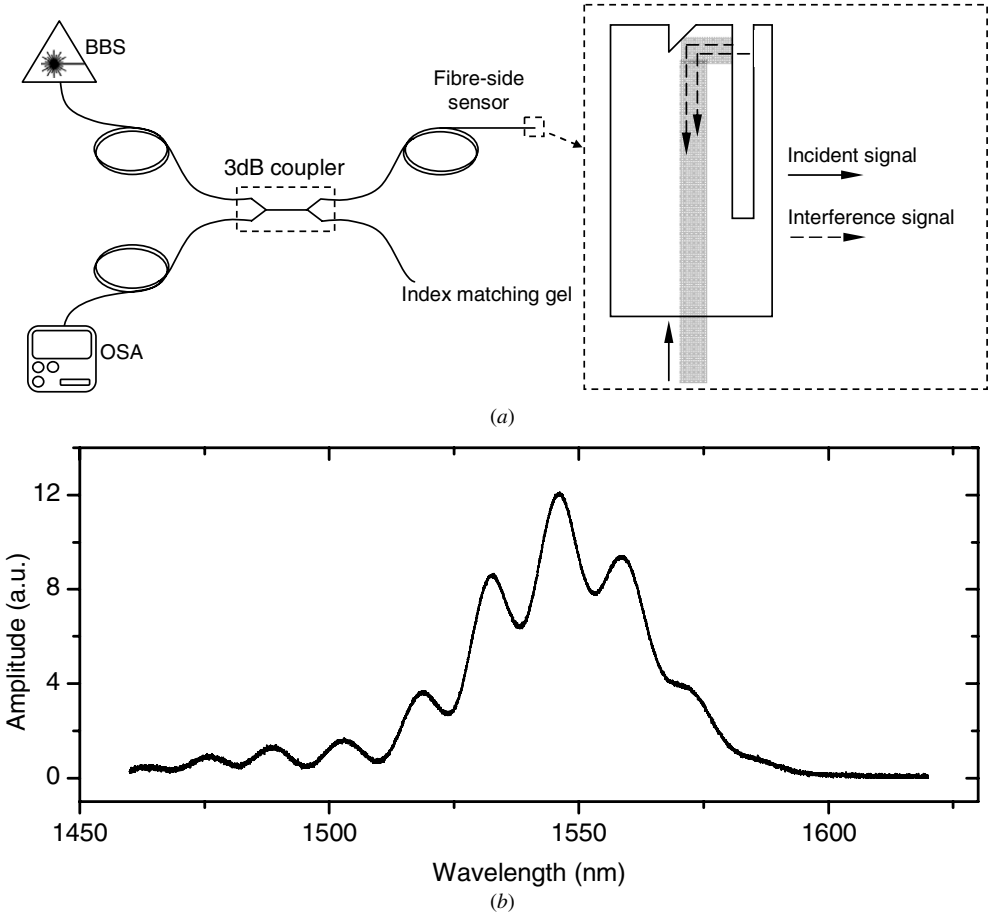

Figure 8. A performance test on the fibre-side optical fibre. (*a*) A sketch of the readout apparatus and the principle of the optical fibre device; (*b*) the original interference signal read out from the fibre-side optical fibre.

to be naturally embedded into this function. The velocity on the moving front $v_\perp$can be obtained by solving the following equation:

$$\begin{cases} v_\perp(x, y, t)|\nabla\phi(x, y, t)| + \phi_t(x, y, t) = 0 \\ \phi(x, y, t = 0) = \Gamma \end{cases}, \tag{6}$$

where Γ is a customized initial state of the level set function. The moving front evolution can be deduced by monitoring certain level set[5] of the level set function.

[5] In this work, the moving front is embedded in the zero level set.

In the FIB machining process, the velocity $v_\perp$ is determined by two parts: (i) the flux of sputtered atoms directly caused by the incident ion beam and (ii) the flux of redeposition atoms [34]:

$$v_\perp = \frac{1}{N} \times [F_{in} \times Y(\theta) \times \cos(\theta) + S_c \times F'], \tag{7}$$

where N is the is the atom density of target material (atoms μm^{-3}); F_{in} is the total incident flux at the target point (x, y); the angular distribution of the sputter yield is $Y(\theta)$ where θ is the ion incident angle; S_c is the sticking coefficient

of the redeposited atoms and F' is the total flux caused by redeposition effect.

In our application, the level set method has been applied in a surface topography model to simulate the contribution from the beam tail effect in the ion polishing process. The moving front represents the cross-sectional profile of the reflective mirror. The simulation imitated a beam of ions with a kinetic energy of 30 keV bombarded onto a fused silica substrate in an incident angle of 45°. In this simulation program the ion current was set at 1 nA. In the surface topography evolution process, the time step and the grid size were set to 2 μs and 1 nm, respectively. In the polishing process, the sputtered atoms are easily able to escape from the open cavity with almost no chance of colliding with the polished surface. Therefore, the redeposition effect can be ignored. This is achieved by setting the sticking coefficient S_c to 0 in the simulation model. The cross-sectional profile of the polished surface is directly embedded in the zero level set in the initial status. Figure 6(*a*) shows the evolution process of the surface polished by a beam of ions along a 45° incident direction. The simulation results show that as the incident ion dose increases, the inclined angle of the polished surface became more close to 45°. Meanwhile, the erosion area is also broadened. Figure 6(*b*) indicates the trend of the inclined angle of the polished sidewall during the machining process. The inclined angle rises from 0° to 40° dramatically in the first 1 ms (per milling pixel). As the scanning time increases, the inclined angle approaches 44.5° and remains constant while the milling depth continues to increase. Therefore, a negative offset on the incident angle of the ion beam can be used to compensate for this effect. According to the simulation result, an offset of 0.5° on the ion incident angle was applied in this experiment.

3.3. Optical performance

The optical fibre was mounted on a mechanical polished block with a 45° inclined angle to measure the surface finish of the reflective mirror using a commercial white light interferometer (Zygo New View 5000) as it is shown in figure 7. The measurement indicated that the surface roughness (Ra) of the reflective mirror formed by the 45° machining process and subsequent application of ~5 nm Pt was 10 nm. This is more than adequate for achieving appropriate optical performance for this application.

A performance test was carried out by coupling the fibre to an optical fibre interferometer readout system as it is shown in figure 8(*a*). In this system, a broad band source (BBS) with a FWHM of 30 nm and a centre wavelength of 1550 nm was used. An optical spectrum analyser (OSA) was employed to record the reflected cavity interference signal. The light incident on the fibre-side cantilever was reflected as shown in figure 8(*a*) with the resulting interference fringes presented in figure 8(*b*). Based on the measurement, the distance between the two parallel sidewalls in the optical cavity can be calculated through fast Fourier transform (FFT) analysis, with typical measurement resolution around 50 nm demonstrated in this case [35].

4. Conclusions

A prototype of a fibre-side optical sensor was successfully fabricated using focussed ion beam machining. It has been demonstrated that a highly accurate reflective mirror (10 μm × 10 μm) with surface roughness (Ra) of 10 nm can be achieved. In the fabrication process, it was also found that for structures requiring a high aspect ratio, the existence of an open edge can mitigate against material redeposition on the sidewalls and therefore increase the overall sputtering rate. In the ion beam polishing process, the surface topography simulation results revealed that the inclined angle of the polished sidewall diverged 0.5° from the incident direction of the ion beam, which is contributed by the beam tail effect. Therefore, a 0.5° offset on the polishing direction is necessary to maintain the machining accuracy. By coupling the fibre to an optical fibre interferometer readout system, interference signals have been successfully captured. The experiment results indicate that the fibre-side optical sensor can be used as a positioning sensor to measure changes in the gap distance on the side of the fibre.

Acknowledgments

The authors gratefully acknowledge the financial support from EPSRC's IMRC at Heriot-Watt University (project no. 113955). This project has been part funded by Renishaw. JL wishes to acknowledge the Scottish Universities Physics Alliance (SUPA) for studentship support.

References

[1] Lee B 2003 Review of the present status of optical fiber sensors *Opt. Fiber Technol.* **9** 57–79
[2] Maier R R *et al* 2004 Temperature dependence of the stress response of fibre Bragg gratings *Meas. Sci. Technol.* **15** 1601
[3] Maier R R *et al* 2010 Distributed sensing using Rayleigh scatter in polarization-maintaining fibres for transverse load sensing *Meas. Sci. Technol.* **21** 094019
[4] Cranch G A, Nash P J and Kirkendall C K 2003 Large-scale remotely interrogated arrays of fiber-optic interferometric sensors for underwater acoustic applications *IEEE Sensors J.* **3** 19–30
[5] Hand D *et al* 1993 Extrinsic Michelson interferometric fibre optic sensor with bend insensitive downlead *Opt. Commun.* **97** 295–300
[6] Tian Z *et al* 2008 Refractive index sensing with Mach–Zehnder interferometer based on concatenating two single-mode fiber tapers *IEEE Photon. Technol. Lett.* **20** 626–8
[7] Kilpatrick J *et al* 2002 Measurement of unsteady gas temperature with optical fibre Fabry–Perot microsensors *Meas. Sci. Technol.* **13** 706
[8] Gander M J *et al* 2003 Embedded micromachined fiber-optic Fabry–Perot pressure sensors in aerodynamics applications *IEEE Sensors J.* **3** 102–7
[9] Iannuzzi D *et al* 2006 Monolithic fiber-top sensor for critical environments and standard applications *Appl. Phys. Lett.* **88** 053501
[10] Iannuzzi D *et al* 2007 Fibre-top cantilevers: design, fabrication and applications *Meas. Sci. Technol.* **18** 3247–52
[11] Kou J *et al* 2010 Microfiber-probe-based ultrasmall interferometric sensor *Opt. Lett.* **35** 2308–10

[12] Nguyen L, Vasiliev M and Alameh K 2011 Three-wave fiber Fabry–Pérot interferometer for simultaneous measurement of temperature and water salinity of seawater *IEEE Photon. Technol. Lett.* **23** 450–2
[13] Volkert C A and Minor A M 2007 Focused ion beam microscopy and micromachining *MRS Bull.* **32** 389–95
[14] Von Bibra M, Canning J and Roberts A 1998 Mode profile modification of H+ ion beam irradiated waveguides using UV processing *J. Non-Cryst. Solids* **239** 121–5
[15] von Bibra M L, Roberts A and Canning J 2001 Fabrication of long-period fiber gratings by use of focused ion-beam irradiation *Opt. Lett.* **26** 765–7
[16] Dhawan A *et al* 2008 Focused ion beam fabrication of metallic nanostructures on end faces of optical fibers for chemical sensing applications *J. Vac. Sci. Technol.* B **26** 2168
[17] Gibson B *et al* 2005 Exposure and characterization of nano-structured hole arrays in tapered photonic crystal fibers using a combined FIB/SEM technique *Opt. Express* **13** 9023–8
[18] Deladi S *et al* 2006 Carving fiber-top optomechanical transducers from optical fibers *J. Micromech. Microeng.* **16** 886–9
[19] Iannuzzi D *et al* 2007 A fiber-top cantilever for hydrogen detection *Sensors Actuators* B **121** 706–8
[20] Iannuzzi D *et al* 2006 Fiber-top atomic force microscope *Rev. Sci. Instrum.* **77** 106105
[21] Tseng A A 2004 Recent developments in micromilling using focused ion beam technology *J. Micromech. Microeng.* **14** 15–34
[22] Guo L J 2004 Recent progress in nanoimprint technology and its applications *J. Phys. D: Appl. Phys.* **37** R123
[23] Vasile M J *et al* 1997 Focused ion beam milling: depth control for three-dimensional microfabrication *J. Vac. Sci. Technol.* B **15** 2350
[24] Vasile M J, Xie J and Nassar R 1999 Depth control of focused ion-beam milling from a numerical model of the sputter process *J. Vac. Sci. Technol.* B **17** 3085
[25] Fu Y and Bryan N K A 2004 Fabrication of three-dimensional microstructures by two-dimensional slice by slice approaching via focused ion beam milling *J. Vac. Sci. Technol.* B **22** 1672
[26] Lalev G *et al* 2008 Data preparation for focused ion beam machining of complex three-dimensional structures *Proc. Inst. Mech. Eng.* B **222** 67–76
[27] Sun J *et al* 2012 A predictive divergence compensation approach for the fabrication of three-dimensional microstructures using focused ion beam machining *Proc. Inst. Mech. Eng.* B **226** 229–38
[28] Bae H *et al* 2010 Miniature surface-mountable Fabry–Perot pressure sensor constructed with a 45 angled fiber *Opt. Lett.* **35** 1701–3
[29] Fu Y *et al* 2000 Influence of the redeposition effect for focused ion beam 3D micromachining in silicon *Int. J. Adv. Manuf. Technol.* **16** 877–80
[30] 1988 Bradley R M and Harper J M E Theory of ripple topography induced by ion bombardment *J. Vac. Sci. Technol.* A **6** 2390–5
[31] Tridyn-A TRIM simulation code including dynamic composition changes 1984 *Nucl. Instrum. Methods Phys. Res.* B **2** 814–8
[32] Möller W, Eckstein W and Biersack J P 1988 TRIDYN-binary collision simulation of atomic collisions and dynamic composition changes in solids *Comput. Phys. Commun.* **51** 355–68
[33] Sethian J 2000 *Level Set Methods and Fast Marching Methods: Evolving Interfaces in Computational Geometry, Fluid Mechanics, Computer Vision, and Materials Science* (Cambridge: Cambridge University Press)
[34] Sun J *et al* 2012 An investigation of redeposition effect for deterministic fabrication of nanodots by focused ion beam *Precis. Eng.* **36** 31–6
[35] Li J *et al* 2013 Focussed ion beam machining of an in-fibre 45° mirror for fibre end sensors *Proc. SPIE* **8794** 879404